HANDBOOK OF NANOPHYSICS

Nanotubes and Nanowires

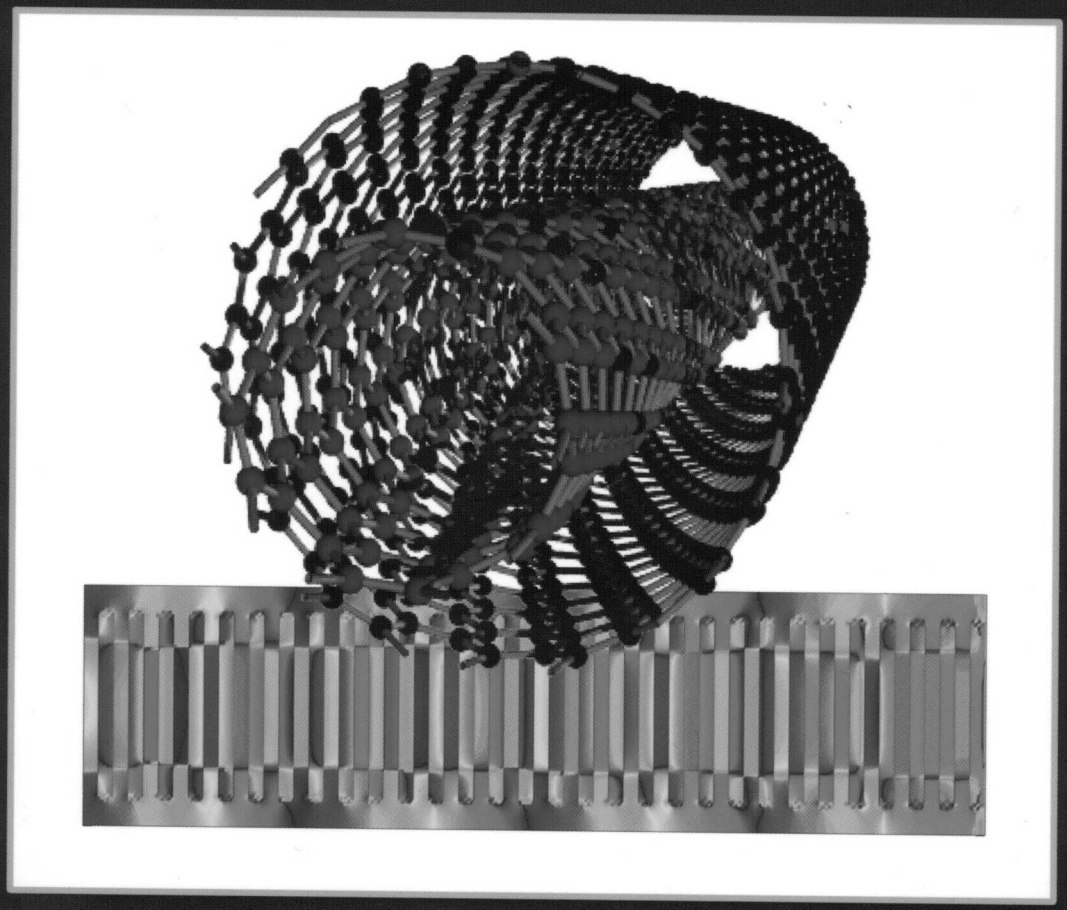

Edited by

Klaus D. Sattler

CRC Press
Taylor & Francis Group

Handbook of Nanophysics

Handbook of Nanophysics: Principles and Methods

Handbook of Nanophysics: Clusters and Fullerenes

Handbook of Nanophysics: Nanoparticles and Quantum Dots

Handbook of Nanophysics: Nanotubes and Nanowires

Handbook of Nanophysics: Functional Nanomaterials

Handbook of Nanophysics: Nanoelectronics and Nanophotonics

Handbook of Nanophysics: Nanomedicine and Nanorobotics

HANDBOOK OF NANOPHYSICS

Nanotubes and Nanowires

Edited by

Klaus D. Sattler

CRC Press
Taylor & Francis Group
Boca Raton London New York

CRC Press is an imprint of the
Taylor & Francis Group, an **informa** business

CRC Press
Taylor & Francis Group
6000 Broken Sound Parkway NW, Suite 300
Boca Raton, FL 33487-2742

Printed in the United States of America on acid-free paper
10 9 8 7 6 5 4 3 2 1

International Standard Book Number: 978-1-4200-7542-7 (Hardback)

Library of Congress Cataloging-in-Publication Data

Handbook of nanophysics. Nanotubes and nanowires / editor, Klaus D. Sattler.
p. cm.
Includes bibliographical references and index.
ISBN 978-1-4200-7542-7 (alk. paper)
1. Nanotubes. 2. Nanowires. I. Sattler, Klaus D. II. Title: Nanotubes and nanowires.

TA418.9.N35N35777 2009
620'.5--dc22 2009038058

Visit the Taylor & Francis Web site at
http://www.taylorandfrancis.com

and the CRC Press Web site at
http://www.crcpress.com

Contents

PART II Inorganic Nanotubes

PART III Types of Nanowires

PART IV Nanowire Arrays

PART V Nanowire Properties

Physics

HANDBOOK OF NANOPHYSICS

Nanotubes and Nanowires

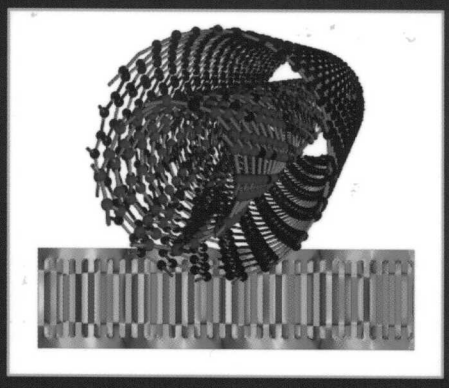

Intensive research on fullerenes, nanoparticles, and quantum dots in the 1990s led to interest in nanotubes and nanowires in subsequent years. **Handbook of Nanophysics: Nanotubes and Nanowires** focuses on the fundamental physics and latest applications of these important nanoscale materials and structures. Each peer-reviewed chapter contains a broad-based introduction and enhances understanding of the state-of-the-art scientific content through fundamental equations and illustrations, some in color.

This volume first covers key aspects of carbon nanotubes, including quantum and electron transport, isotope engineering, and fluid flow, before exploring inorganic nanotubes, such as spinel oxide nanotubes, magnetic nanotubes, and self-assembled peptide nanostructures. It then focuses on germanium, gallium nitride, gold, polymer, and organic nanowires and their properties. The book also discusses nanowire arrays, nanorods, atomic wires, monatomic chains, ultrathin gold nanowires, and several nanorings, including superconducting, ferromagnetic, and quantum dot nanorings.

Nanophysics brings together multiple disciplines to determine the structural, electronic, optical, and thermal behavior of nanomaterials; electrical and thermal conductivity; the forces between nanoscale objects; and the transition between classical and quantum behavior. Facilitating communication across many disciplines, this landmark publication encourages scientists with disparate interests to collaborate on interdisciplinary projects and incorporate the theory and methodology of other areas into their work.

7542X

CRC Press
Taylor & Francis Group
an **informa** business
www.crcpress.com

6000 Broken Sound Parkway, NW
Suite 300, Boca Raton, FL 33487
270 Madison Avenue
New York, NY 10016
2 Park Square, Milton Park
Abingdon, Oxon OX14 4RN, UK

ISBN: 978-1-4200-7542-7
90000
9 781420 075427

www.crcpress.com

III

Types of Nanowires

16

Germanium Nanowires

Sanjay V. Khare
The University of Toledo

Sunil Kumar R. Patil
The University of Toledo

Suneel Kodambaka
University of California

16.1 Introduction

In a nanowire (NW), the momentum of an electron is confined in two directions, thus allowing for electron motion only in one direction (a NW is a one degree of freedom structure and is often called a one-dimensional nanostructure if its diameter is less than 100 nm). This reduction in dimensionality results in dramatic quantum effects dependent on wire material, axis orientation, length, and diameter. These quantum effects in NWs change the electrical, chemical, and mechanical properties to name but a few. Thus, NWs exhibit properties and applications very different from their bulk form. Therefore, they have been assiduously studied recently by experimentalists and theorists for their potential applications in electronic devices and sensors. Investigations for a thorough theoretical understanding of the structure–property relationship for many NWs and NW devices are currently in progress across scientific and engineering disciplines. This research is being carried out on the theoretical side by a multi-scale approach to the atomic simulation of these materials. On the experimental side, a careful study of growth, characterization, and device assembly is ongoing. This chapter gives a brief introduction to this twofold approach. Ample references for further study are also provided. This chapter is divided into five sections. Section 16.2 briefly reviews an elementary NW model derived from the steady-state (time-independent) Schrödinger equation. The aim of this section is to show the profound effect dimensionality has on the electronic properties of a nanostructure. Section 16.3 reviews some Ge NW growth experiments and measurements of Ge NW properties. The electrical, optical, mechanical, and surface properties of Ge NW along with their applications are dealt with briefly in Section 16.4. Section 16.5 introduces some of the simulation methods used to study NWs and describes their capabilities and limits and Section 16.6 forms the conclusion.

16.2 Conceptual Theoretical Model for Nanowires

In this section, we will work with a fundamental equation of quantum mechanics—the time-independent Schrödinger equation (TISE), for the energy eignenfunction $\psi(x,y,z)$ of the electron and its solutions in different dimensions. Effects of these solutions on the electronic properties of NWs will be elucidated. This section is heavily influenced by the presentations in the articles by Harrison (Harrison 1999) and Chen (Chen and Shakouri 2002), which are valuable for exploring this topic further. The three-dimensional (3D) TISE for a constant effective mass is

$$-\frac{\hbar^2}{2m^*}\nabla^2\psi(x,y,z) + V(x,y,z)\psi(x,y,z) = E\,\psi(x,y,z)$$
$$\text{with } \hbar \equiv h/(2\pi), \tag{16.1}$$

where
h is the universal Planck's constant
E is the energy
m^* is the effective mass of the electron

Assuming in the plane dispersion and axis of the wire along the x axis that the total potential $V(x,y,z)$ can be written as a sum of a two-dimensional (2D) confinement potential and a potential along the axis of the wire

$$V(x,y,z) = V(x) + V(y,z), \tag{16.2}$$

and eigenfunction can be written as

$$\psi(x,y,z) = \psi(x)\psi(y,z). \tag{16.3}$$

By substituting Equations 16.2 and 16.3 in Equation 16.1, we get

$$-\frac{\hbar^2}{2m^*}\left[\psi(y,z)\frac{\partial^2\psi(x)}{\partial x^2}\psi(x)\frac{\partial^2\psi(y,z)}{\partial y^2} + \psi(x)\frac{\partial^2\psi(y,z)}{\partial z^2}\right] + \psi(x)V(y,z)\psi(y,z) + \psi(x)V(x)\psi(y,z) = \psi(x)(E_x + E_{y,z})\,\psi(y,z). \tag{16.4}$$

Associating the kinetic and potential energies on the left-hand side of Equation 16.4 to the corresponding energies on the right-hand side and realizing that $V(x) = 0$ (meaning there is no potential gradient along the wire axis), yields two decoupled equations:

$$-\frac{\hbar^2}{2m^*}\frac{\partial^2\psi(x)}{\partial x^2} = E_x\psi(x), \tag{16.5}$$

and

$$-\frac{\hbar^2}{2m^*}\left[\frac{\partial^2\psi(y,z)}{\partial y^2} + \frac{\partial^2\psi(y,z)}{\partial z^2}\right] + V(y,z)\psi(y,z) = E_{y,z}\psi(y,z). \tag{16.6}$$

The solution to Equation 16.5 is

$$E_x = \frac{\hbar^2 k_x^2}{2m^*}. \tag{16.7}$$

Here k_x is any real number.

Equation 16.6 is the Schrodinger equation for a 2D confinement potential in NWs. The solution to this for different wire shapes is more involved but could be simplified by making some assumptions. Assuming an infinitely deep rectangular NW as shown in Figure 16.1, and taking the potential inside the wire to be zero and the potential outside to be infinity changes Equation 16.6 inside the wire to

$$-\frac{\hbar^2}{2m^*}\left[\frac{\partial^2\psi(y,z)}{\partial y^2} + \frac{\partial^2\psi(y,z)}{\partial z^2}\right] = E_{y,z}\psi(y,z). \tag{16.8}$$

Outside the wire, the eigenfunction $\psi(x, y, z) = 0$, since the potential is infinite. Using separation of variables

$$\psi(y,z) = \psi(y)\psi(z), \tag{16.9}$$

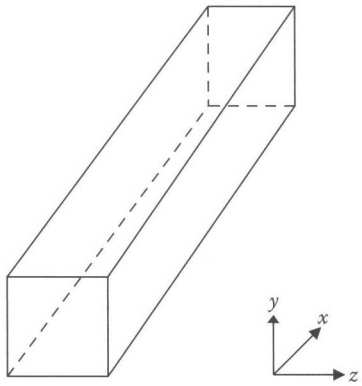

FIGURE 16.1 Infinitely long rectangular nanowire with the potential inside taken to be $V = 0$ and outside as infinity. (Adapted from Harrison, P., *Quantum Wells, Wires and Dots*, John Wiley & Sons, West Sussex, U.K., 1999.)

and substituting Equation 16.9 in Equation 16.8 and assigning the proper energies along the different axes, yields two decoupled equations again:

$$-\frac{\hbar^2}{2m^*}\frac{\partial^2\psi(y)}{\partial y^2} = E_y\psi(y), \tag{16.10}$$

$$-\frac{\hbar^2}{2m^*}\frac{\partial^2\psi(z)}{\partial z^2} = E_y\psi(z). \tag{16.11}$$

The solutions for Equations 16.10 and 16.11 with the origin at a corner and the wire dimensions shown in Figure 16.1 is

$$\psi(y) = \sqrt{\frac{2}{L_y}}\sin\left(\frac{\pi n_y y}{L_y}\right), \quad \psi(z) = \sqrt{\frac{2}{L_z}}\sin\left(\frac{\pi n_z z}{L_z}\right), \tag{16.12a}$$

where n_x and n_y are restricted to be positive integers with components of energy as

$$E_y = \frac{\hbar^2\pi^2 n_y^2}{2m^* L_y^2}, \quad E_z = \frac{\hbar^2\pi^2 n_z^2}{2m^* L_z^2}. \tag{16.12b}$$

The condition that the eigenfunction be zero at the boundary of the wire leads to the quantization of these energy values through the integers n_x and n_y. So spatial charge density distributions that are proportional to $|\psi(y,z)|^2$ are described by two principal quantum numbers, n_y and n_z, as seen in Equation 16.12a. Thus, the confinement energy decreases as the size of the NW increases, due to the presence of the L terms in the denominators in Equation 16.12b. We emphasize that these energies are quantized as a consequence of the integer values n_y and n_z.

16.2.1 Density of States

The electronic density of states (DOS) $D(E)$ is the number of states per unit of energy per unit of volume of real space and is an important quantity. This quantity primarily determines many

physical and chemical properties of materials. It gives us the number of possible energy states, like the ones shown in Equation 16.12, which are allowed to be occupied by electrons. Thus

$$D(E) = \frac{dN}{dE}. \tag{16.13}$$

N is sometimes called the cumulative or total density of states upto an energy E. For bulk material, the three degrees of freedom for electron momentum maps out a sphere in k-space. In quantum wells with two degrees of freedom, the electron momenta fill successively larger circles. For a NW with just one degree of freedom, the electron momenta then fill states along a line. So in one dimension (1D), the total number of states, N^{1D}, is equal to the ratio of the length of the line in k-space ($2k$, for positive and negative values of k) to the length occupied by one state divided by the length in real space, which is L. The factor 2 in the equation accounts for spin degeneracy (i.e., the up and down spin allowed for each electronic state).

$$N^{1D} = 2(2k)\left(\frac{L}{2\pi}\right)\left(\frac{1}{L}\right) = \frac{2k}{\pi}. \tag{16.14}$$

The density of states for NWs can then be derived as

$$D(E)^{1D} = \frac{dN^{1D}}{dE} = \frac{dN^{1D}}{dk}\frac{dk}{dE}. \tag{16.15}$$

From Equation 16.7,

$$\frac{dk}{dE} = \left(\frac{2m^*}{\hbar^2}\right)^{\frac{1}{2}} \frac{E^{\frac{-1}{2}}}{2}. \tag{16.16}$$

Differentiating Equation 16.14 with respect to k and substituting the result and Equation 16.16 in Equation 16.15 yields

$$D(E)^{1D} = \left(\frac{2m^*}{\hbar^2}\right)^{\frac{1}{2}} \frac{E^{\frac{-1}{2}}}{\pi}.$$

Similar calculations may be carried out in 0 dimension (0D; i.e., for a quantum dot), 2D, and 3D. Table 16.1 shows the dependence

TABLE 16.1 Density of States for 1D, 2D, and 3D Nanostructures

Dimensionality	Density of States, $D(E)$
3D	$\left(\frac{2m^*}{\hbar^2}\right)^{\frac{3}{2}} \frac{E^{\frac{1}{2}}}{2\pi^2}$
2D	$\left(\frac{2m^*}{\hbar^2}\right)^{1} \frac{E^{0}}{2\pi}$
1D	$\left(\frac{2m^*}{\hbar^2}\right)^{\frac{1}{2}} \frac{E^{\frac{-1}{2}}}{\pi}$

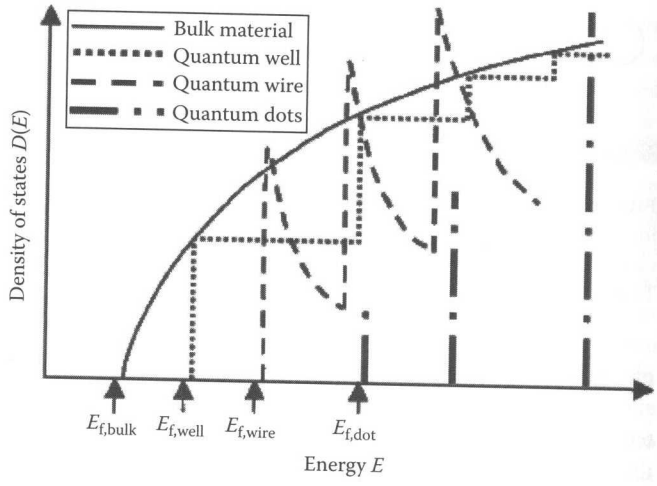

FIGURE 16.2 Density of states of different nanostructures compared to bulk material. (Adapted from Chen, G. and Shakouri, A., *J. Heat Transfer T ASME*, 124, 242, 2002.)

on energy of the DOS for different dimensionalities. Similar data showing how the density of states changes from bulk (3D), to 2D, 1D, and 0D nanostructures are shown in Figure 16.2. The profound effect of dimensionality is clearly seen in Figure 16.2 and is one of the main reasons for the interest in nanostructures in general and nanowires in particular for electronic and optical device applications. While the DOS is continuous for 3D structures, for 1D or NWs it has sharp spikes at different band edges. This leads to strong signals in many optical and electronic measurements at these energies. Similar effects influence the chemical bonding and mechanical properties of NWs due to the confinement of electrons in 2D.

Having briefly explored one of the motivations for NW applications, we now turn our attention to their synthesis in a laboratory. We now focus our attention mostly on germanium NWs for the remainder of this chapter.

16.3 Growth of Ge Nanowires

NWs are most commonly grown via the vapor–liquid–solid (VLS) process (Wagner and Ellis 1964). The VLS process, first proposed in the early 1960s for the growth of Si wires using Au (Wagner et al. 1964b, Wagner and Doherty 1966, Wagner 1967a,b), involves the dissociative adsorption of material from the vapor phase via a low-melting alloy liquid as a catalyst. The preferential incorporation of the material at the solid substrate-catalyst liquid interface leads to growth in the form of cylindrical pillars or "wires." A schematic of the wire growth process is shown in Figure 16.3. In this process, the wire length is determined by the growth flux and the deposition time while the wire diameter is controlled by the catalyst size. Using VLS, wires as long as a few millimeters and as narrow as a few nanometers wide, have been grown (Cui et al. 2001, Park et al. 2008). To date, a wide variety of materials (elemental metals, semiconductors as well as compound arsenides, borides, carbides, nitrides, oxides,

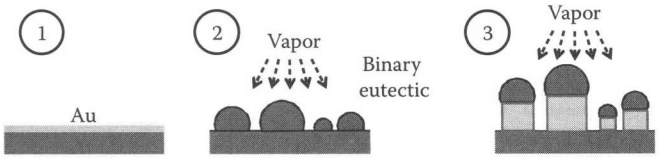

FIGURE 16.3 Schematic of vapor–liquid–solid process. Au is shown in panel (1), half-circles in panel (2), and (3) at the top of the wires are Au catalysts. Bottom region is the substrate. (Adapted from Kodambaka, S., Tersoff, J., Ross, M.C., and Ross, F.M., *Proc. SPIE*, 7224, 72240C, 2009.)

phosphides, selenides, sulphides, and tellurides) have been successfully grown in the form of whiskers or NWs using this technique (Givargizov 1978). Readers are encouraged to refer to the article by Givargizov (1987) for an excellent review of the entire list of materials grown, methods employed, catalysts, and growth parameters used.

Interest in the semiconducting NWs stems from their potential for applications in a wide variety of areas ranging from opto- and nano-electronics to chemical and biological sensors (Haraguchi et al. 1992, Duan et al. 2000, Cui and Liueber 2001, Bjork et al. 2002, Gudiksen et al. 2002, DeFranceschi et al. 2003). More recently, Si and Ge NWs have attracted considerable attention owing to their significantly enhanced energy storage and energy generation properties (Tian et al. 2007, Boukai et al. 2008, Chan et al. 2008a,b, Hochbaum et al. 2008). Here, we focus on the Au-catalyzed growth of Ge NWs and the influence of growth parameters such as substrate temperature, source flux, and catalyst state (solid or liquid) on the morphological and structural evolution of the NWs.

The growth of Ge using Au was first reported four decades ago (Wagner et al. 1964a) and more recently using other metals such as Ti (Wan et al. 2003), Ni (Tuan et al. 2005), and Mn (Lensch-Falk et al. 2007). It is interesting to note that the Au-catalyzed VLS growth of Si occurs at temperatures T that are above the bulk Au–Si eutectic temperature T_E = 363°C (Okamoto and Massalski 1986) while Au-catalyzed Ge wire growth has been reported to occur at T as low as 260°C (Miyamoto and Hirata 1975, Wang and Dai 2002, Kamins et al. 2004, Adhikari et al. 2006, Jin et al. 2006) i.e., ~100 K below the bulk Au–Ge eutectic temperature T_E = 361°C (see Figure 16.4) (Okamoto and Massalski 1986).

However, until recently, the exact growth mechanisms were not clear. This is because most existing studies focused on post-growth characterization to determine the growth processes. While *ex situ* characterization is essential for the determination of chemical composition, interface structure, and wire morphologies, inference of the growth mechanisms from such data is difficult. *In situ* observations permit the direct determination of the growth rates and hence the kinetics and help identify several aspects of the VLS growth process that have not been previously discussed.

In this section, we review the recent *in situ* transmission electron microscopy (TEM) studies of Ge NW growth kinetics as a means of developing a fundamental understanding of their growth

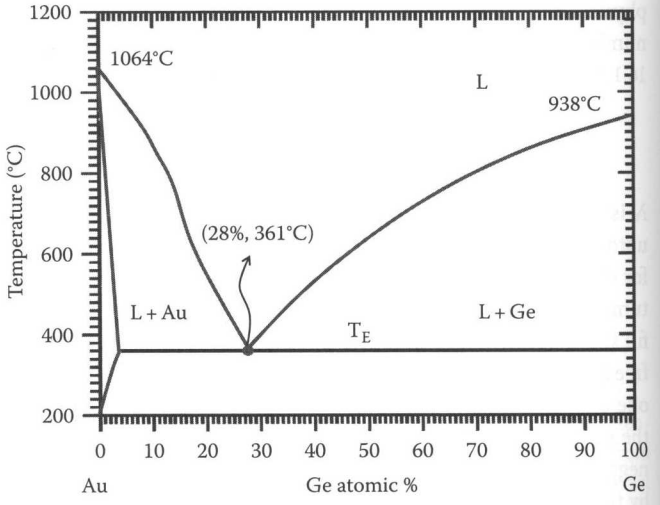

FIGURE 16.4 Au-Ge phase diagram. (Adapted from Okamoto, H. and Massalski, T.B., *Binary Alloy Phase Diagrams* I, ASM International, Gaithersburg, MD, 1986.)

mechanisms. TEM images of the wires and the catalyst droplets are collected at video rate as a function of the growth pressure, temperature, and gas environment. From the images, the wire growth rates were measured, the catalyst states were identified, and the rate-limiting steps were determined. Ge wire growth, as shown in the following sections, occurs in the presence of a liquid catalyst at temperatures below the bulk AuGe alloy eutectic temperature. This liquid phase, key to the successful growth of Ge wires, is found to be stable only at high Ge concentrations.

All the experimental results pertaining to Ge NW growth experiments were carried out at the IBM T. J. Watson Research Center in a multi-chamber UHV (base pressure 2×10^{-10} Torr) transmission electron microscope (300 kV Hitachi H-9000 TEM) equipped with *in situ* physical and chemical vapor deposition (CVD) facilities. First, Si(111) wafers (miscut < 0.5°) were sliced into 1.5 × 4 × 0.5 mm sections, cleaned chemically, and mounted in the TEM with the polished surface vertical. The samples were degassed in the UHV at 600°C for 2 h followed by annealing at 1250°C for 30–60 s. Au thin films, 2–3 nm thick, were deposited at room temperature by thermal evaporation from a Knudsen cell at a rate of 3×10^{-3} nm/s onto the samples in a preparation chamber at a base pressure of 2×10^{-8} Torr during the deposition. These Au-covered Si(111) samples were then transferred under the UHV to the TEM chamber and wire growth was initiated by resistively heating the samples in a gas mixture (purity 99.999%) containing 80% He and 20% of digermane (Ge_2H_6) for the growth of Ge NWs, respectively. Prior to deposition, the samples were first annealed in vacuum at ~400°C for 5 min and then cooled to the growth temperatures T < 350°C. As soon as the samples are heated, eutectic droplets form and act as the catalysts for the formation of individual wires. NW growth is initiated beneath these eutectic droplets and the wires grow away from the surface, most of which are perpendicular to the substrate and hence are imaged with the electron beam perpendicular to the wire axis. Individual wires can be observed in bright or dark fields in

transmission mode, and the effects of the pressure, temperature, and gas environment can be observed directly.

Ge wires are observed to grow at Ge_2H_6 pressures $P > 9 \times 10^{-7}$ Torr and temperatures between 300°C and 380°C. The maximum pressure in these experiments is limited to 10^{-5} Torr by the design of the TEM. The gases are leaked continuously into the microscope column to ensure a constant pressure during wire growth. Under these conditions, ⟨111⟩-oriented Ge wires that are several hundreds of nanometers long can be grown for times between 1 and 6 h. TEM images are acquired at video rate (30 frames/s). Wires grown under continuous, as well as intermittent, electron beam irradiation exhibit similar growth rates indicating that the electron beam does not affect the wire growth kinetics. Substrate temperatures are measured before and after the deposition using an infrared pyrometer. After growth, the surface can be cleaned by heating to 1250°C, so that a series of growth experiments can be carried out on the same sample in one area. For such a series, the relative temperature can be measured to within 20 K, while for different samples the measurement uncertainties in absolute temperature are ~50 K.

In these experiments, the Ge_2H_6 pressure range accessible for growth was between 1×10^{-7} and 1×10^{-5} Torr. Sustained epitaxial growth of the ⟨111⟩-oriented single-crystalline Ge wires was observed at 250°C < T < 400°C. In contrast to Si, Ge wires are bounded by smooth sidewalls. Figure 16.5 is a typical bright field TEM image of Ge NWs obtained during deposition at T = 330°C using 4.8×10^{-6} Torr Ge_2H_6.

Note that the wire tips show smoothly curved catalyst particles indicative of the liquid phase and suggest that the Ge wires grow via the VLS process. This is an important observation since T_E = 361°C for AuGe alloy (see Figure 16.4) while liquid droplets are observed at T = 330°C.

In order to understand the Ge wire growth kinetics, a series of experiments were carried out while systematically varying the substrate temperature and Ge_2H_6 pressure during growth.

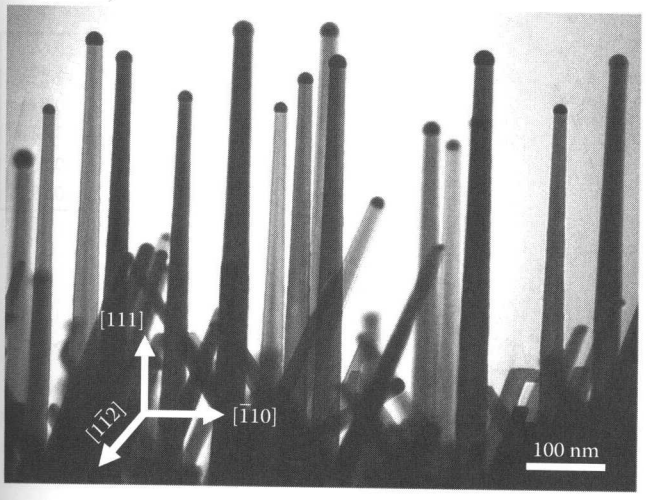

FIGURE 16.5 A typical bright-field TEM image obtained from a Si(111) sample during the VLS growth of Ge nanowires. Most wires grow epitaxially in the ⟨111⟩ direction. (Adapted from Kodambaka, S., Tersoff, J., Ross, M.C., and Ross, F.M., *Proc. SPIE*, 7224, 72240C, 2009.)

In one such experiment, the effect of the substrate temperature on the AuGe catalyst state was studied during wire growth at a constant Ge_2H_6 pressure. Solidification of the droplets occurred at temperatures far below (~100 K) T_E and required significantly higher temperatures (>400°C) to re-establish the liquid phase. This hysteresis in the solid–liquid phase transformation is seen in all Ge growth experiments and for wires with a range of diameters (20–140 nm). Interestingly, the wires continue to grow even after the catalyst particle has solidified, i.e., via the vapor–solid–solid (VSS) process. Measurements made on several wires showed that VSS growth is 10–100 times slower than VLS growth at the same Ge_2H_6 pressure and temperature, presumably due to weaker surface reactivity and/or lower diffusivity through the solid. Both VLS and VSS growth were observed to occur simultaneously on neighboring wires in some instances. All the wires, irrespective of the growth mode, are crystalline and the only obvious difference between the growth modes is that VSS process yields more tapered wires owing to their relatively slower growth rates. This demonstration of dual growth modes may be relevant to the controversy regarding the role of VSS and VLS growth in other systems (Persson et al. 2004, Harmand et al. 2005).

The growth experiments carried out while varying Ge_2H_6 pressure at a constant substrate temperature showed that a significant Ge_2H_6 pressure appears to be essential for stabilizing the liquid state below T_E. Whenever the Ge_2H_6 pressure is reduced during VLS growth, the solidification of catalyst droplets was observed (see Figure 16.6).

Here, the first image shows a typical VLS-grown Ge wire. In this experiment, growth was initiated using 4.6×10^{-6} Torr Ge_2H_6 and continued at pressures $\geq 1.1 \times 10^{-6}$ Torr for ~78 min. The Ge_2H_6 pressure was then reduced to 2.8×10^{-7} Torr while maintaining a constant temperature. Within 681 s, the droplet abruptly solidifies. The fact that the droplets can solidify confirms that the temperature is definitely below the bulk T_E, independent of any uncertainties in temperature calibration.

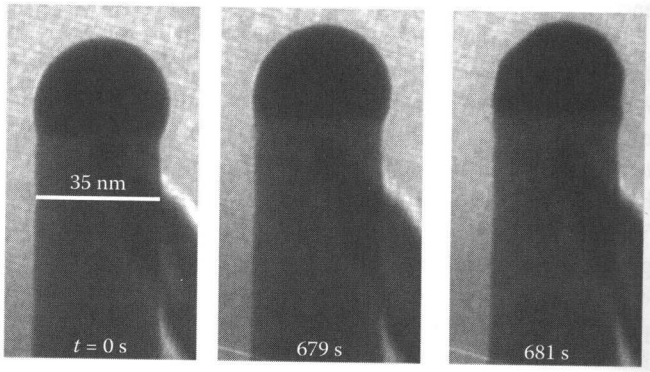

FIGURE 16.6 Representative bright-field TEM image series showing the solidification of AuGe catalyst on top of a Ge wire when the Ge_2H_6 pressure is reduced during growth at a constant temperature T = 340°C. In this experiment, Ge_2H_6 pressure was dropped from 1.1×10^{-6} Torr to 2.8×10^{-7} Torr at t = 0. (Adapted from Kodambaka, S., Tersoff, J., Ross, M.C., and Ross, F.M., *Proc. SPIE*, 7224, 72240C, 2009.)

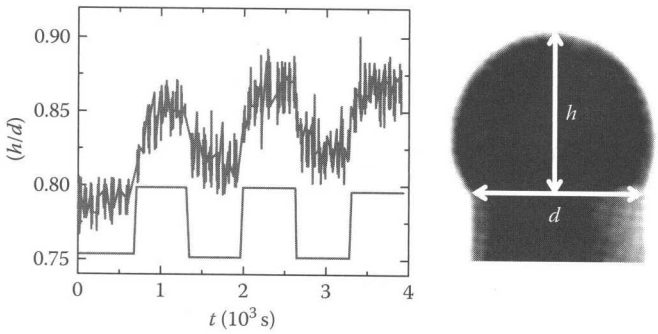

FIGURE 16.7 Plots of aspect ratio (top curve) of a AuGe eutectic droplet on top of a Ge wire (diameter = 59 nm) and Ge_2H_6 pressure (bottom curve) vs. t at $T = 355°C$. The data is acquired from a TEM video sequence as the pressure is cycled repeatedly between 1.9×10^{-6} Torr and 8.4×10^{-6} Torr. Aspect ratio (h/d) is defined as the ratio of the height h and the base width d of the droplet as labeled on the TEM image. (Adapted from Kodambaka, S. et al., *Science*, 316, 729, 2007.)

This behavior is typical of all droplets observed, although the exact time delay between smaller and larger droplets depends on the growth history and in some cases can be as long as several tens of minutes.

In order to understand the role of Ge_2H_6 pressure on the droplet state, shapes of AuGe droplets were measured during wire growth as a function of Ge_2H_6 pressure at a constant T. Figure 16.7 is a typical plot of the aspect ratio of a droplet as the pressure is varied repeatedly between higher and lower values.

Although the changes are small, note that when the Ge_2H_6 pressure is decreased, the aspect ratio decreases and when the Ge_2H_6 pressure is increased, the aspect ratio increases. Clearly, the droplet shape is varying with Ge_2H_6 pressure, suggesting that there are observable changes in surface energy with pressure (Kodambaka et al. 2007). All the above observations suggest that the liquid phase may be effectively stabilized against solidification by Ge supersaturation, which arises from the growth process (Kodambaka et al. 2007). For more details, the reader is encouraged to refer to the article by Kodambaka et al. (2007).

In conclusion, *in situ* TEM experiments enable the quantitative determination of the NW growth mechanisms. In case of Au-catalyzed growth of Ge NWs, it was found that the AuGe catalyst state may be either solid or liquid below the bulk eutectic temperature, with the state depending not just on temperature but also on the Ge_2H_6 pressure and history. Remarkably, both VLS and VSS processes can operate under the same conditions to grow Ge wires. Most surprisingly, a significant Ge_2H_6 pressure is essential for growth via the VLS process below the eutectic temperature. Clearly, *in situ* observations provide valuable insights into the physical processes controlling the morphological and structural evolution of NWs and are expected to be general and applicable to other material systems.

Large-scale fabrication of NW-based devices for the above-mentioned applications requires precise control over NW morphology (shape, length, and size), crystalline structure, chemical composition, and interfacial abruptness. This is an extremely challenging task governed by a complex interplay of the thermodynamics of the materials and the kinetics of nucleation and growth processes. For example, growth orientations of Ge wires can be varied between ⟨111⟩, ⟨110⟩, or ⟨112⟩ by changing the growth temperature, precursor, and the growth technique (Hanrath and Korgel 2005). However, very little is known concerning the factors affecting the wire orientation (Tan et al. 2002, Borgström et al. 2004, Wu et al. 2004a, Schmidt et al. 2005, Wang et al. 2006). Despite several years of research in this area, none of the following has been achieved, even for relatively simple elemental Si and Ge NWs: (1) ⟨100⟩-oriented Si or Ge wires, (2) Si/Ge heterostructures with atomically-abrupt interfaces (Clark et al. 2008), or (3) large-scale synthesis of sub-5 nm diameter wires. Success in the rational synthesis of NWs with desired architecture can only be achieved through a fundamental understanding of all the processes influencing the nucleation and growth.

16.4 Properties of Ge Nanowires

Having looked at the VLS growth of Ge NWs, we turn to their properties and applications. NWs could be the building blocks for the post-CMOS era bottom-up assembly of nano devices. The primary requirements for this new technological era are compatibility with traditional silicon manufacturing processes and integration for cost reduction. For this reason, Ge is the front runner to replace silicon. Ge has a lighter effective mass for the electron and hole charge carriers than Si implying higher carrier mobilities and thus high-performance transistors. Figure 16.8, adapted from the article by Yu (Yu et al. 2006), shows that bulk Ge has direct (~0.88 eV) and indirect (~0.66 eV) band gaps making it an attractive material for electronic and photonic circuitry applications. These band gaps can be further tuned for specific electronic/photonic applications by controlling the wire

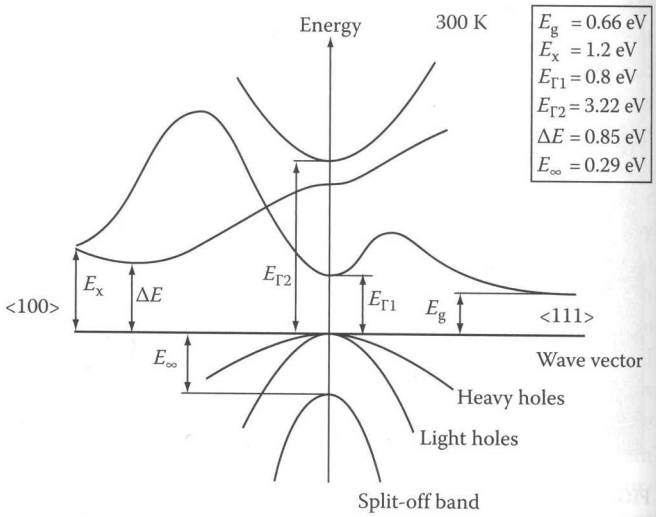

FIGURE 16.8 Band gaps in bulk Ge. (Adapted from Yu, B. et al., *J. Clust. Sci.*, 17, 579, 2006.)

dimensions thus giving rise to a myriad of design possibilities. Some of the quantum effects leading to various properties and applications for Ge NWs are discussed here.

16.4.1 Structural Properties

For NWs, the surface to volume ratio is very large. This leads to the surface reconstruction of the atoms in the NW as seen in Figure 16.9, which shows the simulated Ge NWs with H termination of the structures adapted from Medabonia et al. (2007). After analyzing bond lengths in these structures, Medaboina et al. observed that bond lengths between Ge atoms at the surface were relaxed by ~1%, whereas no relaxation was observed for atoms in the interior region away from the surface. When the NWs were allowed to dimerize, it was observed that the atoms relaxed by ~50% as expected. Cross-sections of wires along [110] were found to have cylindrical structures for all diameters. Along the [001] and [111] axes, the smaller wires with diameters $d < dc$ have circular cross-sections. As seen from Figure 16.9, the critical diameter dc, above which the cross-section acquires a faceted shape, lies in the range of 2.0 nm < dc < 3.0 nm for [001] and [111] axes. The value of dc is determined by the competition to lower the total energy between the energies of the different exposed surfaces of H terminated Ge under the constraint of a fixed volume. Wires along the [001] direction appear in Figure 16.9 to have a rectangular bonding geometry rather than the expected square surface arrangement of atoms in a single [001] surface layer. This expected square arrangement of atoms of a diamond lattice is not made of the nearest neighbor atoms. The rectangular structure seen in Figure 16.9 arises because the middle atoms, along the longer side of the rectangle, are the nearest neighbors of the top layer atoms and are one layer below the top layer. For larger diameters, $d > dc = 2.15$ nm wires along [001], cross-sections were found to be octagonal-shaped with facets of the [001] and [110] type, which were normal to [001]. For larger diameters, $d > dc = 2.11$ nm wires along [111], they were hexagonal-shaped with facets of the [110] type, which were normal to [111]. Thus, we see that the arrangement of atoms of a NW cut along a particular direction depends on its diameter, its axis orientation, and the termination of its surface. We will see in the following discussion that the properties of a NW are intimately related to its crystal structure.

16.4.2 Electronic Properties and Applications

As seen from Equation 16.12, the quantum confinement of electrons (in the NW cross-section) leads to the difference between successive energy states to increase as NW diameter decreases. This leads to an increase in the band gap between the filled and unoccupied electronic energy states, which correspondingly increases with a decreasing diameter. For example, in InP NWs, it was found that the band gap E_g varies with diameter d of the wires as $E_g \sim 1/d^{1.45}$. Simple particle in box type explanations (as shown in Section 16.2) though qualitatively adequate, do not account for this scaling quantitatively (Yu et al. 2003). As expected from previous theoretical analysis, Figure 16.10 shows the dependence of the band gap of hydrogen passivated Ge NWs

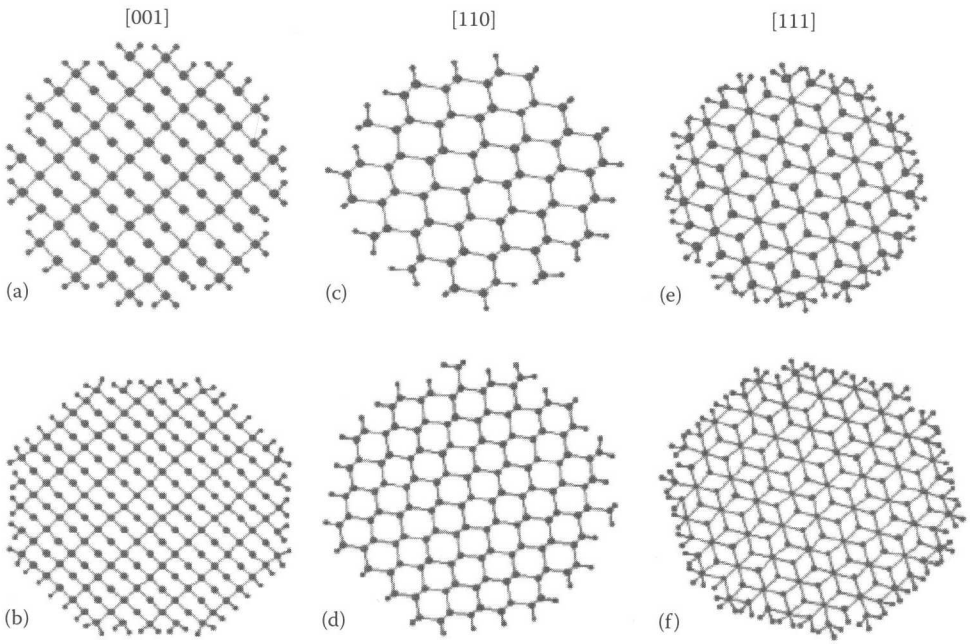

FIGURE 16.9 Cross-sectional views of the relaxed Ge NWs. (a) $NW_{[001]}^{(Ge\text{-}89,H\text{-}44)}$ (2.03), (b) $NW_{[001]}^{(Ge\text{-}185,H\text{-}60)}$ (3.03), (c) $NW_{[110]}^{(Ge\text{-}69,H\text{-}32)}$ (2.12), (d) $NW_{[110]}^{(Ge\text{-}133,H\text{-}40)}$ (3.3), (e) $NW_{[111]}^{(Ge\text{-}170,H\text{-}66)}$ (2.11), (f) $NW_{[111]}^{(Ge\text{-}326,H\text{-}90)}$ (3.03). Larger circles represent Ge atoms and the outer smaller ones represent the H atoms used to saturate dangling bonds. Local geometrical patterns corresponding to the axis of the wires are evident: square shapes for [001] axis, hexagonal for [110], and parallelograms for [111]. (Adapted from Medaboina, D. et al., *Phys. Rev. B*, 76, 205327, 2007.)

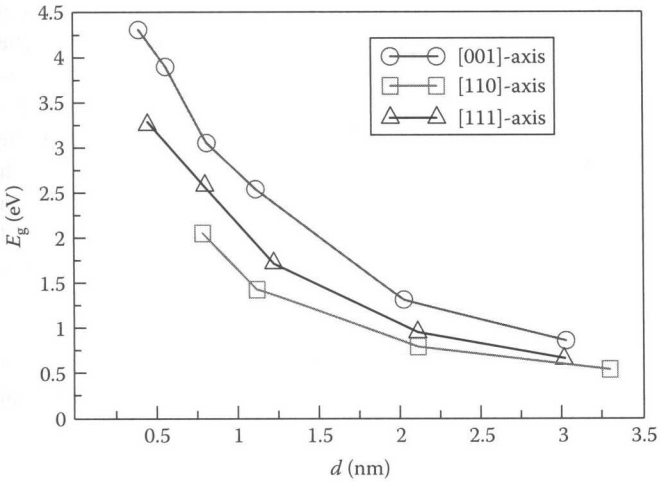

FIGURE 16.10 Dependence of band gap on the wire diameter and orientation. (Adapted from Medaboina, D. et al., *Phys. Rev. B*, 76, 205327, 2007.)

on their diameter and orientation (Medaboina et al. 2007). Band structures for different Ge NWs (shown in Figure 16.9) as calculated by Medaboina et al. are shown in Figure 16.11. As expected, the band structure varies depending on the wire orientation, diameter, and passivation material. The dispersion of the valence band for wires with approximately the same diameter is greatest for wires along [110] and least for wires along [111]. As expected from a quantum size effect, Figure 16.11 shows the absolute value of the valence band maximum decreases in energy and the absolute value of the conduction band minimum increases in energy as the thickness of the wire decreases. This leads to an increase in the electronic band gap with a decreasing NW diameter. The band gap could be either direct or indirect, depending on the crystallographic orientation. NWs along [110] and thin ($d < 1.3$ nm) ones along [001] have direct band gaps occurring at the gamma point. This is different from bulk Ge band structure as shown in Figure 16.8. Such wires, due to their direct gaps, would be suitable for applications in optics. Wires along [001] were found to transit from direct to indirect band gaps as the diameter increased above 1.3 nm, while all wires along [111] had indirect band gaps. Another important factor used to control the electronic properties of NWs is doping. Dopants of *n*- and *p*-type in NWs are required for faster and low power consuming logic devices. Doping has been studied in several NWs and has been used to design inverters, LEDs, and bipolar transistors. Obtaining good electronic properties for *n*- and *p*-channel FETs is more complicated (Greytak et al. 2004). Band bending caused by doping Ge NWs has been demonstrated experimentally (Wang and Dai 2006). Figure 16.12 shows the simulation results of band structures of doped ~2 nm diameter Ge NWs for a single wire along each crystallographic direction [001], [110], and [111]. A high level of doping (0.5%–1.5%) obviously has an impact on the electronic structures of Ge NWs. As shown in Figure 16.12, adding a *p*-type (*n*-type) dopant moves the Fermi energy toward the valence band (conduction band). The maximum of the valence band and the minimum of the conduction band increase

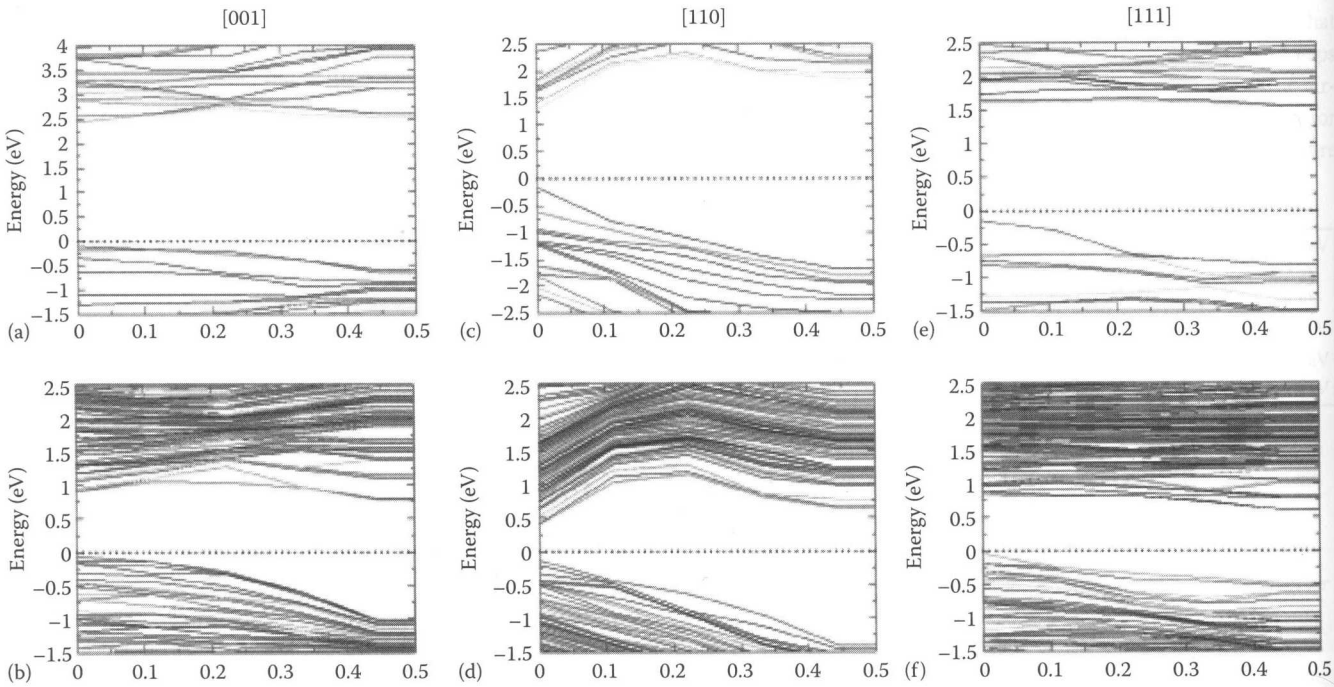

FIGURE 16.11 Band Structure of Ge NW along [001], [110], and [111] directions. The Fermi level in each panel is set to zero and is shown by the dotted line. (a) $NW_{[001]}^{(Ge\text{-}25,H\text{-}20)}$ (1.12) and (b) $NW_{[001]}^{(Ge\text{-}185,H\text{-}60)}$ (3.03) represent the band structure along the [001] direction. (c) $NW_{[110]}^{(Ge\text{-}17,H\text{-}12)}$ (1.12) and (d) $NW_{[110]}^{(Ge\text{-}133,H\text{-}40)}$ (3.3) represent the band structure along the [110] direction. (e) $NW_{[111]}^{(Ge\text{-}62,H\text{-}42)}$ (1.23) and (f) $NW_{[111]}^{[Ge\text{-}326,H\text{-}90]}$ (3.03) represent the band structure along the [111] direction. (Adapted from Medaboina, D. et al., *Phys. Rev. B*, 76, 205327, 2007.)

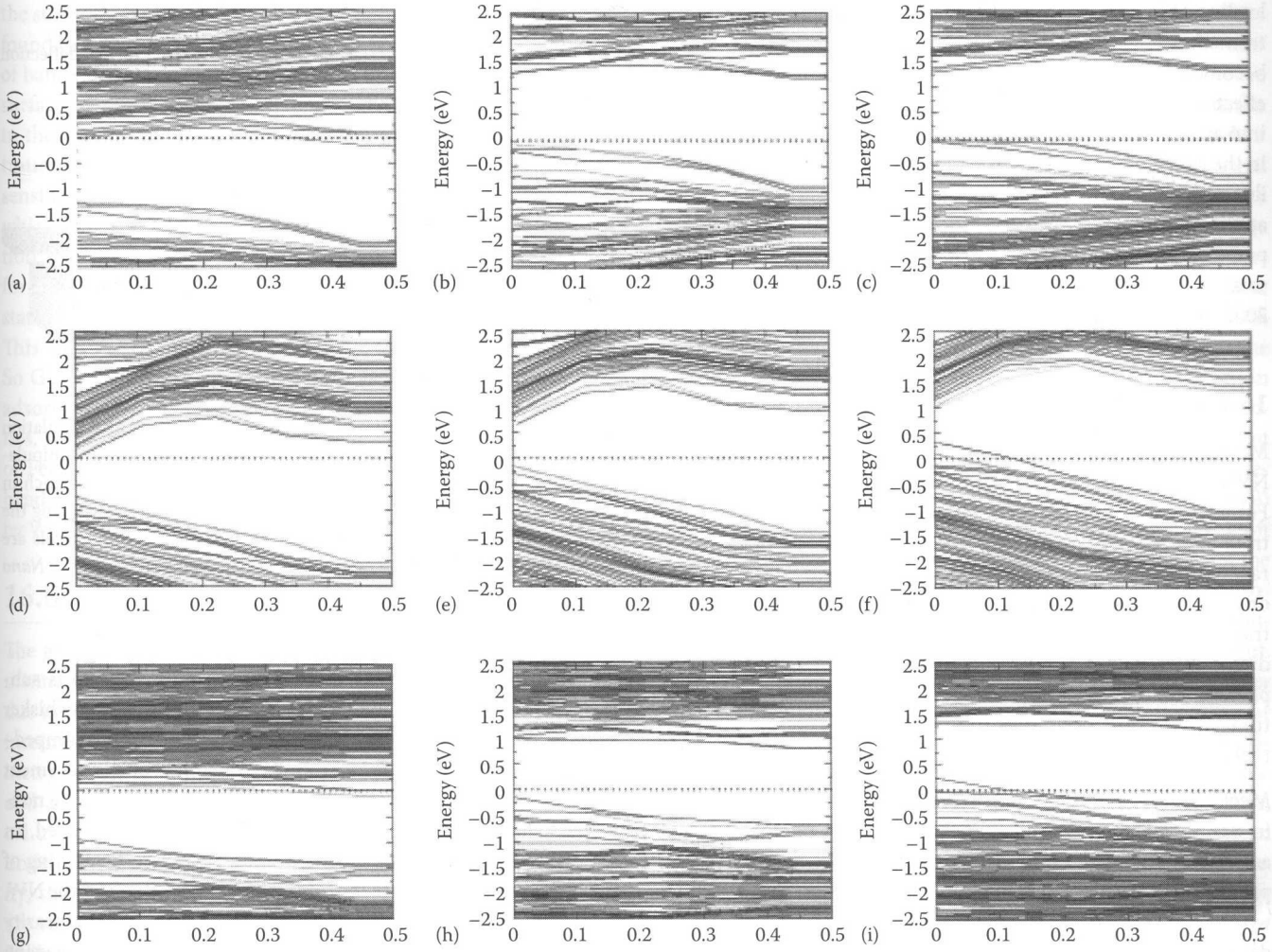

FIGURE 16.12 Comparison of band structures of Ge NWs with and without doping. The Fermi level in each panel is set to zero and is shown by the dotted line. (a) $NW_{[001]}^{(Ge\text{-}88,H\text{-}44,P\text{-}1)}$ (2.03), (d) $NW_{[110]}^{(Ge\text{-}68,H\text{-}32,P\text{-}1)}$ (2.12), and (g) $NW_{[111]}^{(Ge\text{-}169,H\text{-}66,P\text{-}1)}$ (2.11) are *n*-type doped wires. (b) $NW_{[001]}^{(Ge\text{-}89,H\text{-}44)}$ (2.03), (e) $NW_{[110]}^{(Ge\text{-}69,H\text{-}32)}$ (2.12), and (h) $NW_{[111]}^{(Ge\text{-}170,H\text{-}66)}$ (2.11) are undoped wires. (c) $NW_{[001]}^{(Ge\text{-}88,H\text{-}44,B\text{-}1)}$ (2.03), (f) $NW_{[110]}^{(Ge\text{-}68,H\text{-}32,B\text{-}1)}$ (2.12), and (i) $NW_{[111]}^{(Ge\text{-}169,H\text{-}66,B\text{-}1)}$ (2.11) are *p*-type doped wires. (Adapted from Medaboina, D. et al., *Phys. Rev. B*, 76, 205327, 2007.)

(decrease) in energy with the addition of *p*-type (*n*-type) dopant when measured relative to the Fermi level. Figure 16.12 also shows that the doping of wires does not have a significant effect on the dispersion of valence and conduction bands. Thus, the effect of doping on the band structure of hydrogenated Ge NWs is similar to that in doped bulk Ge. This property would make Ge NWs suitable for applications that require the tuning of the NW conductivity by doping.

Ge NW-FETs are ideal for very-low-power circuit applications. The majority of the published work (Yu et al. 2006) shows that Ge NW-FETs function at nano- to micro-amperes on-state current with a large on-to-off current ratio (10^4–10^6). The switching energy of a single-NW-FET is 3 to 6 orders of magnitude lower than that of a typical top-down conventional FET. The standby power is almost negligible due to the pA-level off-state leakage per NW. These excellent properties make Ge NW-FETs an ideal nano electric device for micro or nano power chips with significantly improved power performance tradeoff (Yu et al. 2006).

16.4.3 Optical Properties and Applications

Germanium's compatibility with Group III–V materials and germanium oxide's optical properties allow for the realization of radical integrated optoelectronic circuitry designs. Photoluminescence (Canham 1990, Duan et al. 2000, Katz et al. 2002) data revealed a substantial blue shift with a decreasing size of NWs. It has also been shown recently that Ge NWs could be used in optoelectronic components fabricated within silicon-based technology (Halsall et al. 2002). Optical properties of NWs also mainly depend on the size of the wire, orientation of the wire (Bruno et al. 2007), and passivation material and doping utilized (Wu et al. 2004b). As explained earlier, the band gap and band structure change with wire size and orientation

leading to numerous ways of obtaining a particular optoelectronic functionality. The simulation of optical properties of NWs becomes expensive if the proper incorporation of many body effects like self energy, local field, and excitonic effects are taken into account correctly (Bruno et al. 2005). Ge NWs of diameters in the range of 0.8 nm have the main absorption peak in the visible range (Bruno et al. 2007), which could lead to an efficient application of Ge NWs in optoelectronic devices when compared with Si NWs. Already, Ge NW-based nano devices like solar cells, magnets (Alguno et al. 2003), and FETs (Wang et al. 2003) have been characterized.

16.4.4 Mechanical Properties and Applications

Mechanical stability: The high surface to volume ratio of NWs gives them interesting mechanical properties, as well. For example, simulations on Au NWs show that a spontaneous transition from face centered cubic (fcc) to body centered tetragonal (bct) structure occurs in ⟨001⟩ oriented gold (Au) NWs or cross-sections less than $4\,nm^2$. The simulations showed no transitions when the wires were oriented along ⟨111⟩ or ⟨110⟩ directions (Diao et al. 2003). It may be speculated that similar phenomena driven by surface reconstruction may cause structural phase transitions into the interior of Ge NWs. However, there has been no such observation to date.

Mechanical strength: If NWs are to be used as building blocks in nano devices, their mechanical properties need to be characterized for avoiding mechanical failure. With current NW production techniques, NWs can be grown as single crystals with the absence of any structural defects such as point or line defects. This sometimes leads to the high mechanical strength and stiffness of NWs close to their theoretical single crystal limits (Wong et al. 1997, Diao et al. 2003, Kis et al. 2003).This property makes them attractive for use in composites and nano-electromechanical devices. Many test set-ups have been used to characterize the mechanical properties of NWs. Figure 16.13 shows the most commonly used clamped beam experimental set-up for lateral loading of the Ge NW bending test using a atomic force microscope (AFM). Despite the widespread use of the clamped beam configuration, a comprehensive model that accounts for the detailed shape of these force-displacement (F-d) curves over the entire elastic region is yet to be described and validated for NW systems. Heidelberg et al. (2006) provides a method for the complete description of the elastic properties in a double-clamped beam configuration over the entire elastic regime for diverse wire systems. This method can be used to perform a comprehensive analysis of F-d curves using a single closed-form analytical description. It can be applied to extract linear material constants such as the Young's modulus (E) and to describe the entire elastic range and hence to identify the yield points for dramatically different systems of NWs. The same set-up and theory have been used for tests on Ge NWs (Ngo et al. 2006) of sizes between 20 and 80 nm. These tests revealed that the bulk moduli of NWs is comparable with that of bulk Ge but their mechanical strength

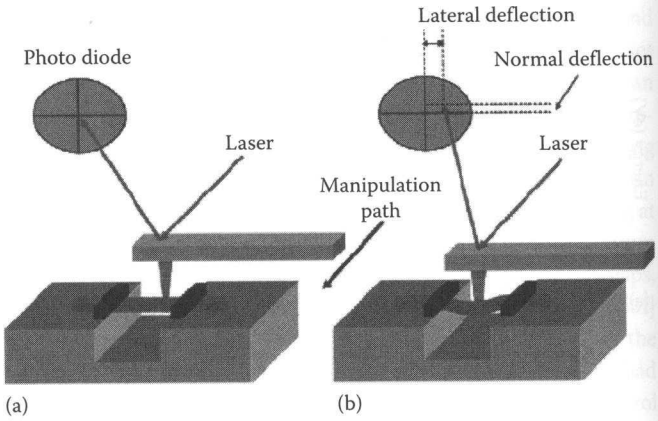

FIGURE 16.13 Schematic of the lateral nanowire manipulation experiment setup: (a) before manipulation, (b) during manipulation. The nanowire under investigation is suspended over a trench in the substrate and fixed by Pt deposits at the trench edges. During the manipulation the lateral and normal cantilever deflection signals are simultaneously recorded. (Adapted from Heidelberg, A. et al., *Nano Lett.*, 6, 1101, 2006.)

is closer to the theoretical value for pure bulk Ge and is substantially greater than the mechanical strength of any whisker semiconductor. Simple bending stress analysis on the clamped-clamped beam system shows a linear variation of displacement with force (Heidelberg et al. 2006). This cannot explain the nonlinear behavior seen in Figure 16.13. As the NW is displaced, an axial tensile force is inherently induced due to the stretching of the NW. This force affects the total stress experienced by the NW, leading to an enhancement of its rigidity and thus non-linearity of the F-d curve. The curve fit to the elastic deformation plot using the closed-form solution (Heidelberg et al. 2006) gives a Young's modulus of 137.6 GPa and a fracture strength of 17.1 GPa. An important observation is that the Ge NW breaks without plastic deformation, revealing its brittle nature.

16.4.5 Surface Chemistry and Applications

Two commonly occurring adsorbents for Si and Ge surfaces are hydrogen and oxygen. An adsorbent layer on a surface can significantly affect the surface reconstruction and also lead to faceting or de-faceting transitions of the surface. Density functional theory (DFT) computations (Mingwei et al. 2006) show that the passivation of Ge NWs with more stable ethine reduces the quantum confinement effects when compared with that of Ge NWs passivated with hydrogen. NWs have been thought to be the active elements in sensing devices because the large surface area is believed to cause the sensitive dependence of electronic properties on changes in surface adsorption by different chemical species (Wang and Dai 2006). Ge NWs along [111], which have facets of [110] and [100] types have been studied (Medaboina et al. 2007) by changing the surface hydrogen concentration. This orientation has the tendency of the unhydrogenated facets to dimerize. Hydrogen atoms were removed from

the surface of relaxed wires. Band structures of these wires were found to have electronic states with energies lying in the middle of band gap due to the occurrence of unpaired electrons on the surface of the NW after the removal of H atoms. This change in the electronic properties with a change in hydrogen concentration for wires along [111] could be potentially exploited in sensing applications, due to the disappearance of the band gap, which would cause a significant increase in electronic conduction. Synthesized Ge NWs could be oxidized when exposed to air forming Ge/GeO_2 surfaces leading to the high density of surface states causing appreciable Fermi level pinning (Kingston 1957). This oxidation phenomenon is more severe for small wires. So Ge NWs have to be chemically passivated with appropriate adsorbents to avoid the degradation of their electronic properties. Band bending could occur in Ge NWs due to the pinning of Fermi level at surface states (Wang et al. 2004, 2005). Band bending due to surface oxidation of Ge NWs has been explored by Wang and Dai (Wang and Dai 2006).

16.5 Simulation Methods

The grand challenge of producing complex nanodevices by elementary nano building blocks still faces several hurdles. NWs due to the nano-length scale along one axis also show properties intermediate between bulk and single atoms. This broken symmetry means quantum mechanical computations are expensive and a multi-scale approach is necessary. A thorough theoretical understanding of the properties of nano structures involves understanding the issues of their symmetry, lower dimensionality, size, and chemical composition. Computational techniques are very useful to deal with the multiplicity of these parameters. Table 16.2 lists some of the simulation methods that have been commonly used to characterize nanostructures. All these theoretical techniques attempt to solve complex body problems arising due to the interaction between different atoms. Moving down the table increases assumptions employed in the theory thus simplifying the model and decreasing the fidelity of the result, the advantage being reduced computational cost. The simulation method that would yield the best results in a reasonable amount of time differs from case to case and is entirely at the discretion of the user. For the interested reader, Martin (2004) gives additional information of these simulation methods. Quantum Monte Carlo (QMC) simulations approximate the many electron solutions by a wave function obtained from Monte Carlo methods. Many types of QMC (Hammond et al. 1992) techniques are available for various applications. These simulations are very expensive and so are limited to few tens of atoms. In DFT, the many-electron system is approximated by functionals that depend on spatial electron density. DFT (Thomas 1927, Hohenberg and Kohn 1964, Kohn and Sham 1965, Parr and Yang 1989, Fiolhais et al. 2003) has been a workhorse in condensed matter physics with comparatively less computational expense than QMC. After the exchange and correlation interaction effects were added to DFT (Kohn and Sham 1965), it has also been used in computational chemistry with improved results. Some of the disadvantages of DFT include the difficulty of accounting for the exchange and correlation effects in strongly correlated materials like high temperature superconductors. Specifically as related to NWs, DFT methods do not account correctly for electron–hole interactions that could become appreciable for small NWs (Bruno et al. 2007). In tight binding (TB) methods (Turchi et al. 1997, Slater and Koster 1954, Ashcroft and Mermin 1976, Goringe et al. 1997), the Hamiltonian of the many-body system is approximated as the Hamiltonian of an isolated center at each lattice point and the resultant atomic orbitals are assumed to become localized within a lattice constant. These assumptions make the computational solution to larger systems with many atoms less expensive. In classical molecular dynamics (MD) simulations, the many atom problem is approximated by a potential or force field between atoms or molecules. MD (McCammon and Harvey 1987, Haile 2001, Oren et al. 2001, Schlick 2002) is generally used when interaction effects between thousands of atoms or molecules are of interest. It is very commonly used in large material systems and bio-molecule (or large protein) simulations.

TABLE 16.2 Hierarchy of Computational Simulation Methods Used for Studying Nanostructures

Quantum Monte Carlo (QMC)
GW
Time dependent density functional theory
Time independent density functional theory (DFT)
Tight binding (TB)
Classical molecular dynamics (MD)

Note: Going down the column increases the physical assumptions in the input parameters, but yields computation-time savings leading to large scale simulations.

16.6 Conclusions

We have shown a rudimentary theory connecting the physical dimensions of a NW to its properties. We have described state-of-the-art Ge NW growth techniques. TEM characterization of the growth process was reported. A brief overview of the effect of Ge NW diameter, orientation, passivation, and doping on surface reconstruction, band gap, and band structure has been provided. The resulting electrical, optical, mechanical, and surface properties have been explained and their applications have been cited. Different nanoscale simulation techniques used for the numerical analysis of NW were briefly listed. Ge NWs have a considerable potential for next generation microelectronics, photonics, and nanodevices owing to their high carrier mobilities, tenability of their band gaps, and recently discovered high mechanical strength at NW scales. This chapter should serve as a quick reference for Ge NW growth methods, properties, and applications.

Acknowledgments

SVK thanks the NSF, DARPA, Wright Center for PVIC from the State of Ohio, Wright Patterson Air Force Base, and Kirtland Air Force Base for funding this work.

References

Adhikari, H., Marshall, A.F., Chidsey, C.E.D., and McIntyre, P.C. 2006. Germanium nanowire epitaxy: Shape and orientation control. *Nano Lett.* 6: 318–323.

Alguno, A., Usami, N., Ujihara, T., Fujiwara, K., Sazaki, G., and Nakajima, K. 2003. Enhanced quantum efficiency of solar cells with self-assembled Ge dots stacked in multilayer structure. *Appl. Phys. Lett.* 83: 1258.

Ashcroft, W. and Mermin, N.D. 1976. *Solid State Physics*, Brooks Cole, Belmont, CA.

Bjork, M.T., Ohlsson, B.J., Thelander, C. et al. 2002. Nanowire resonant tunneling diodes. *Appl. Phys. Lett.* 81: 4458–4460.

Borgström, M., Deppert, K., Samuelson, L., and Seifert, W.J. 2004. Size- and shape-controlled GaAs nano-whiskers grown by MOVPE: A growth study. *J. Cryst. Growth* 260: 18–22.

Boukai, A.I., Bunimovich, Y., Tahir-Kheli, J., Yu, J.-K., Goddard III, W.A., and Heath, J.R. 2008. Silicon nanowires as efficient thermoelectric materials. *Nature* 451: 168–171.

Bruno, M., Palummo, M., Marini, A. et al. 2005. Excitons in germanium nanowires: Quantum confinement, orientation, and anisotropy effects within a first-principles approach. *Phys. Rev. B* 72: 153310.

Bruno, M., Palummo, M. Ossicinic, S., and Del Sole, R. 2007. First-principles optical properties of silicon and germanium nanowires. *Surf. Sci.* 601: 2707.

Canham, L.T. 1990. Silicon quantum wire array fabrication by electrochemical and chemical dissolution of wafers. *Appl. Phys. Lett.* 57: 01046.

Chan, C.K., Peng, H., Liu, G. et al. 2008a. High-performance lithium battery anodes using silicon nanowires. *Nat. Nanotechnol.* 3: 31–35.

Chan, C.K., Zhang, X.F., and Cui, Y. 2008b. High capacity Li ion battery anodes using Ge nanowires. *Nano Lett.* 8: 307–309.

Chen, G. and Shakouri, A. 2002. Heat transfer in nanostructures for solid-state energy conversion. *J. Heat Transfer–T ASME* 124: 242–252.

Clark, T.E., Nimmatoori, P., Lew, K.-K., Pan, L., Redwing, J.M., and Dickey, E.C. 2008. Diameter dependent growth rate and interfacial abruptness in vapor–liquid–solid $Si/Si_{1-x}Ge_x$ heterostructure nanowires. *Nano Lett.* 8: 1246–1252.

Cui, Y., Lauhon, L.J., Gudiksen, M.S., Wang, J., and Lieber, C.M. 2001. Diameter-controlled synthesis of single-crystal silicon nanowires. *Appl. Phys. Lett.* 78: 2214–2216.

Cui, Y. and Lieber, C.M. 2001. Functional nanoscale electronic devices assembled using silicon nanowire building blocks. *Science* 291: 851–853.

De Franceschi, S., J van Dam, A., Bakkers, E.P.A.M., Feiner, L.F., Gurevich, L., and Kouwenhoven, L.P. 2003. Single-electron tunneling in InP nanowires. *Appl. Phys. Lett.* 83: 344–346.

Diao, J.K., Gall, K., and Dunn, M.L. 2003. Surface-stress-induced phase transformation in metal nanowires. *Nat. Mater.* 2: 656.

Duan, X., Wang, J., and Lieber, C.M. 2000. Synthesis and optical properties of gallium arsenide nanowires. *Appl. Phys. Lett.* 76: 01116.

Fiolhais, C., Nogueira, F., and Marques, M. 2003. *A Primer in Density Functional Theory*, Springer-Verlag, Berlin, Germany.

Givargizov, E.I. 1978. Growth of whiskers by VLS mechanism. *Curr. Top. Mater. Sci.* 1: 82–145.

Givargizov, E.I. 1987. *Highly Anisotropic Crystals*. Springer-Verlag, Berlin, Germany.

Goringe, C.M., Bowler, D.R., and Hernández, E. 1997. Tight-binding modelling of materials. *Rep. Prog. Phys.* 60: 1447.

Greytak, A.B., Lauhon, L.J., Gudiksen, M.S., and Lieber, C.M. 2004. Growth and transport properties of complementary germanium nanowire field-effect transistors. *Appl. Phys. Lett.* 84: 4176.

Gudiksen, M.S., Lauhon, L.J., Wang, J., Smith, D.C. and Lieber C.M. 2002. Growth of nanowire superlattice structures for nanoscale photonics and electronics. *Nature* 415: 617–620.

Haile, M. 2001. *Molecular Dynamics Simulation: Elementary Methods*, Wiley Professional, New York.

Halsall, P., Omi, H. and Ogino. T. 2002. Optical properties of self-assembled Ge wires grown on Si(113). *Appl. Phys. Lett.* 81: 2448.

Hammond, B.J., Lester W.A., and Reynolds, P.J. 1992. Monte Carlo methods in Ab Initio. *Int. J. Quantum Chem.* 42: 837.

Hanrath, T. and Korgel, B.A. 2005. Crystallography and surface faceting of germanium nanowires. *Small* 1: 717–721.

Haraguchi, K., Katsuyama, T., Hiruma, K., and Ogawa, K. 1992. GaAs p-n-junction formed in quantum wire crystals. *Appl. Phys. Lett.* 60: 745–747.

Harmand, J.C., Patriarche, G., Pere-Laperne, N., Merat-Combes, M.N., Travers, L., and Glas, F. 2005. Analysis of vapor-liquid-solid mechanism in Au-assisted GaAs nanowire growth. *Appl. Phys. Lett.* 87: 203101.

Harrison, P. 1999. *Quantum Wells, Wires and Dots*. John Wiley & Sons, West Sussex, U.K.

Heidelberg, A., Ngo, L.T., Wu, B. et al. 2006. A generalized description of the elastic properties of nanowires. *Nano Lett.* 6: 1101.

Hochbaum, I., Chen, R., Delgado, R.D. et al. 2008. Enhanced thermoelectric performance of rough silicon nanowires. *Nature* 451: 163–167.

Hohenberg, P. and Kohn, W. 1964. Inhomogeneous electron gas. *Phys. Rev. B* 864: 136.

Jin, C.-B., Yang, J.-E., and Jo, M.-H. 2006. Shape-controlled growth of single-crystalline Ge nanostructures. *Appl. Phys. Lett.* 88: 193105.

Kamins, T.I., Li, X., and Williams, R.S. 2004. Growth and structure of chemically vapor deposited Ge nanowires on Si substrates. *Nano Lett.* 4: 503–506.

Katz, D., Wizansky, T., Millo, O., Rothenberg, E., Mokari, T., and Banin, U. 2002. Size-dependent tunneling and optical spectroscopy of CdSe quantum rods. *Phys. Rev. Lett.* 89: 86801.

Kingston, R.H. (ed.) 1957. *Semiconductor Surface Physics*, University of Pennsylvania Press, Philadelphia, PA.

Kis, A., Mihailovic, D., Remskar, M. et al. 2003. Shear and Young's moduli of MoS2 nanotube ropes. *Adv. Mater.* 15: 733.

Kodambaka, S., Tersoff, J., Reuter, M.C. and Ross, F.M. 2007. Germanium nanowire growth below the eutectic temperature. *Science* 316: 729–732.

Kodambaka, S., Tersoff, J., Ross, M.C., and Ross, F.M. 2009. Growth Kinetics of Si and Ge nanowires. *Proc. SPIE* 7224: 72240C.

Kohn, W. and Sham, L.J. 1965. Self-consistent equations including exchange and correlation effects. *Phys. Rev. A* 140:1133.

Lensch-Falk, J.L., Hemesath, E.R., Lopez, F.J., and Lauhon, L.J. 2007. Vapor-solid-solid synthesis of Ge nanowires from vapor-phase-deposited manganese germanide seeds. *J. Am. Chem. Soc.* 129: 10670–10671.

Martin, R.M. 2004. *Electronic Structure: Basic Theory and Practical Methods*, Cambridge University Press, Cambridge, U.K.

McCammon, J.A. and Harvey S.C. 1987. *Dynamics of Proteins and Nucleic Acids*, Cambridge University Press, Cambridge, U.K.

Medaboina, D., Gade, V., Patil, S.K.R., and Khare, S.V. 2007. Effect of structure, surface passivation, and doping on the electronic properties of Ge nanowires: A first principles study. *Phys. Rev. B* 76: 205327.

Mingwei, J., Ming, N., Wei, S. et al. 2006. Anisotropic and passivation-dependent quantum confinement effects in germanium nanowires: A comparison with silicon nanowires. *J. Phys. Chem. B* 110: 18332–18337.

Miyamoto, Y. and Hirata, M. 1975. Growth of new form Germanium whiskers. *Jpn. J. Appl. Phys.* 14: 1419–1420.

Ngo, L.T., Almecija, D., Sader, J.E. et al. 2006. Ultimate-strength germanium nanowires. *Nano Lett.* 6: 2964.

Okamoto, H. and Massalski, T.B. 1986. *Binary Alloy Phase Diagrams* I. ASM International, Gaithersburg, MD.

Oren, M., Alexander, D.M., Benoît, R., and Masakatsu, W. 2001. *Computational Biochemistry and Biophysics*, Marcel Dekker, New York.

Park, W.I., Zheng, G., Jiang, X., Tian, B., and Lieber, C.M. 2008. Controlled synthesis of millimeter-long silicon nanowires with uniform electronic properties. *Nano Lett.* 8: 3004–3009.

Parr, R.G. and Yang, W. 1989. *Density-Functional Theory of Atoms and Molecules*, Oxford University Press, New York.

Persson, A.I., Larsson, M.W., Stenstrom, S., Ohlsson, B.J., Samuelson, L., and Wallenberg L.R. 2004. Solid-phase diffusion mechanism for GaAs nanowire growth. *Nat. Mater.* 3: 677–681.

Schlick, T. 2002. *Molecular Modeling and Simulation*. Springer-Verlag, New York.

Slater, J.C. and Koster, G.F. 1954. Simplified LCAO method for the periodic potential problem, *Phys. Rev.* 94, 1498.

Schmidt, V., Senz, S., and Gösele, U. 2005. Diameter-dependent growth direction of epitaxial silicon nanowires. *Nano Lett.* 5: 931–935.

Tan, T.Y., Lee, S.T., and Gösele, U. 2002. A model for growth directional features in silicon nanowires. *Appl. Phys.* A 74: 423–432.

Tian, B., Zheng, X., Kempa, T.J. et al. 2007. Coaxial silicon nanowires as solar cells and nanoelectronic power sources. *Nature* 449: 885–890.

Thomas, L.H. 1927. The calculation of atomic fields. *Proc. Cam. Philos. Soc* 23: 542.

Tuan, H.Y., Lee, D.C., Hanrath, T. and Korgel, B.A. 2005. Germanium nanowire synthesis: An example of solid-phase seeded growth with nickel nanocrystals. *Chem. Mater.* 17: 5705–5711.

Turchi, P.E., Gonis, A., and Colombo, L. 1997. Tight-binding approach to computational materials science. *Materials Research Society Symposia Proceedings*, vol. 491, Boston, MA.

Wagner, R.S. 1967a. *Crystal Growth*. Pergamon Press, Oxford & New York, pp. 45–119.

Wagner, R.S. 1967b. Defects in silicon crystals grown by VLS technique. *J. Appl. Phys.* 38: 1554–1560.

Wagner, R.S. and Doherty, C.J. 1966. Controlled vapor-liquid-solid growth of silicon crystals. *J. Electrochem. Soc.* 113: 1300–1305.

Wagner, R.S. and Ellis, W.C. 1964. Vapor-liquid-solid mechanism of single crystal growth. *Appl. Phys. Lett.* 4: 89–90.

Wagner, R.S., Doherty, C.J., and Ellis, W.C. 1964a. Preparation + Morphology of crystals of Silicon + Germanium grown by vapor-liquid-solid mechanism. *J. Met.* 16: 761.

Wagner, R.S., Ellis, W.C., Arnold, S.M., and Jackson, K.A. 1964b. Study of filamentary growth of silicon crystals from vapor. *J. Appl. Phys.* 35: 2993–3000.

Wan, Q., Li, G., Wang, T.H., and Lin, C.L. 2003. Titanium-induced germanium nanocones synthesized by vacuum electron-beam evaporation: Growth mechanism and morphology evolution. *Solid State Commun.* 125: 503–507.

Wang, C.X., Hirano, M., and Hosono, H. 2006. Origin of diameter-dependent growth direction of silicon nanowires. *Nano Lett.* 6: 1552–1555.

Wang, D. and Dai, H. 2002. Low-temperature synthesis of single-crystal germanium nanowires by chemical vapor deposition. *Angew. Chem. Int. Ed.* 41: 4783–4786.

Wang, D. and Dai, H. 2006. Germanium nanowires: From synthesis, surface chemistry, and assembly to devices. *Appl. Phys. A: Mater. Sci. Process.* 85: 217.

Wang, D., Chang, Y.L., Wang, Q. et al. 2004. A novel method for preparing carbon-coated germanium nanowires. *J. Am. Chem. Soc.*126: 11602.

Wang, D.W., Tu, R., Zhang, L., Dai, H.J. 2005. Deterministic one-to-one synthesis of germanium nanowires and individual gold nanoseed patterning for aligned arrays. *Angew. Chem. Int. Ed.* 44: 2925.

Wang, D., Wang, W., Javey, A., Tu, R., and Dai, H. 2003. Germanium nanowire field-effect transistors with SiO2 and high-kappa HfO2 gate dielectrics. *Appl. Phys. Lett.* 83: 2432.

Wong, W.W., Sheehan, P.E., and Lieber, C.M. 1997. Nanobeam mechanics: Elasticity, strength, and toughness of nanorods and nanotubes. *Science* 277: 1971.

Wu, Y. Cui, Y., Huynh, L., Barrelet, C.J., Bell, D.C., and Lieber, C.M. 2004a. Controlled growth and structures of molecular-scale silicon nanowires. *Nano Lett.* 4: 433–436.

Wu, J., Punchaipetch, P., Wallace, R., and Coffer, J. 2004b. Fabrication and optical properties of erbium-doped germanium nanowires. *Adv. Mater.* 16: 1444.

Yu, B., Sun, X.H., Calebotta, G.A., Dholakia, G.R., and Meyyappan, M. 2006. One-dimensional germanium nanowires for future electronics. *J. Clust. Sci.* 17: 579.

Yu, H., Li, J., Loomis, R.A., Wang, L.W., and Buhro, W.E. 2003. Two- versus three-dimensional quantum confinement in indium phosphide wires and dots. *Nat. Mater.* 2: 517.